Electronic Supplementary Material (ESI) for Journal of Materials Chemistry C.

Supplementary material

Cobalt-induced structural modulation in multiferroic Aurivillius-phase oxides

V. Koval[1], Y. Shi[2], I. Skorvanek[3], G. Viola[4], R. Bures[1], K. Saksl[1], P. Roupcova[5,6], M. Zhang[4], Ch. Jia[2], and H. Yan[4]

[1]Institute of Materials Research, Slovak Academy of Sciences, Kosice, Slovakia

[2]Key Laboratory for Magnetism and Magnetic Materials of MOE, Lanzhou University, China

[3]Institute of Experimental Physics, Slovak Academy of Sciences, Kosice, Slovakia

[4]School of Engineering and Materials Science, Queen Mary University of London, United Kingdom

[5]Institute of Physics of Materials ASCR, Brno, Czech Republic

[6]CEITEC Brno University of Technology, Brno, Czech Republic

X-ray diffraction analysis

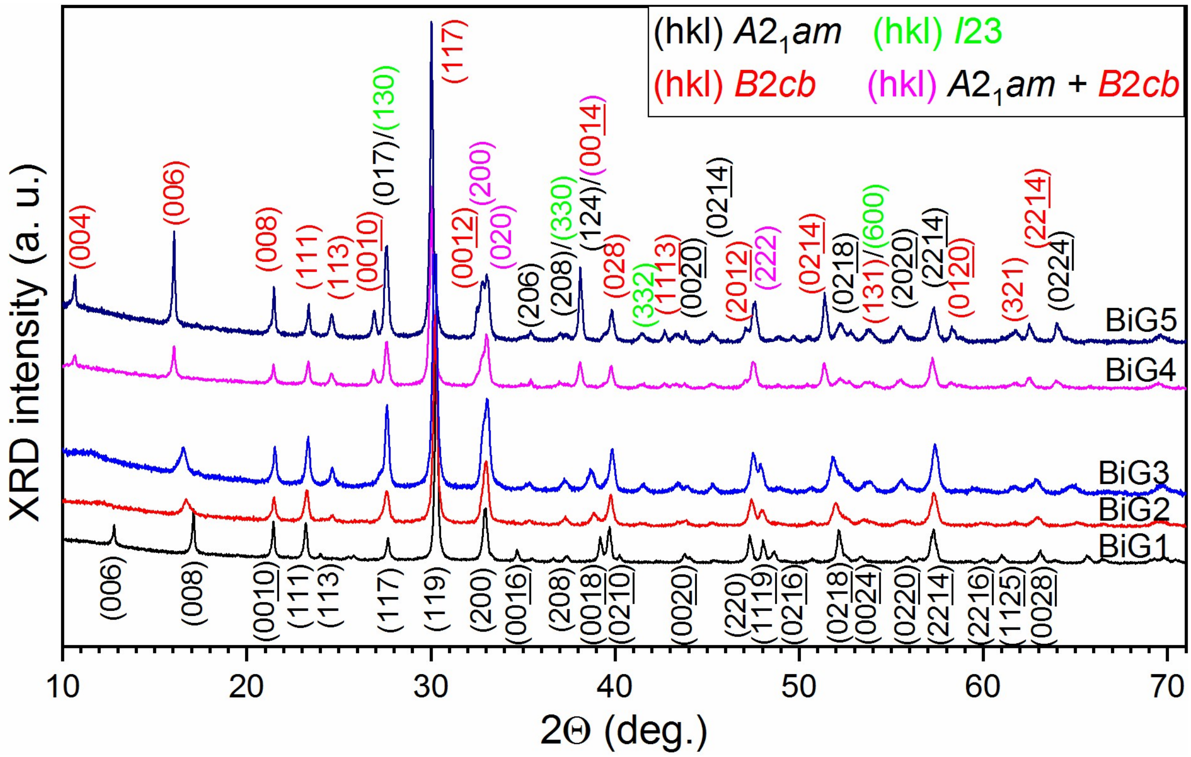

Figure S1. Stack plot of the XRD patterns of the BiG1-BiG5 samples, as recorded at room temperature (black Miller h, k, l indices: orthorhombic *A*2$_1$*am* phase, red indices: orthorhombic *B*2*cb* phase, green indices: cubic *I*23 phase; cyan indices: overlapped peaks of the *A*2$_1$*am* and *B*2*cb* phases).

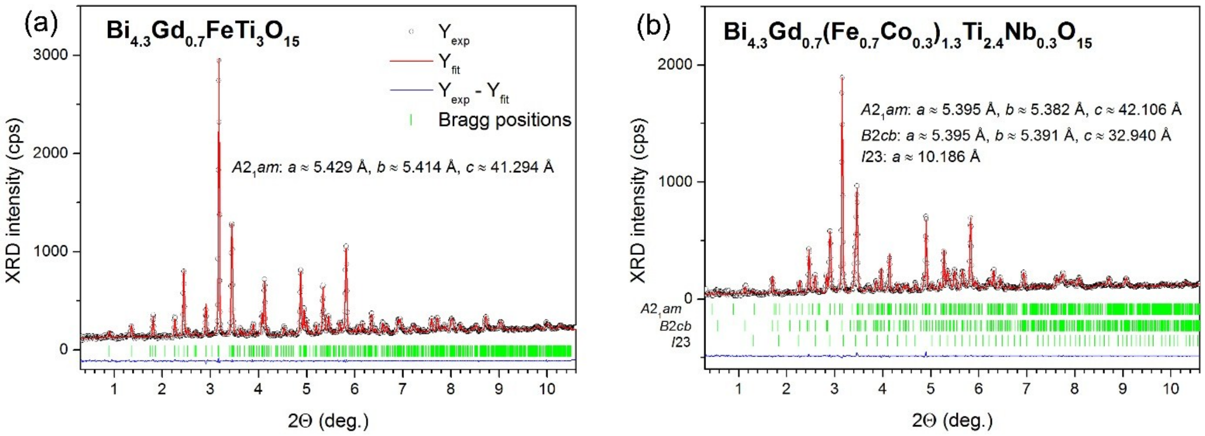

Figure S2. Observed (black open circles), calculated (red solid line) and difference (blue solid line) patterns obtained from the Rietveld analysis of the synchrotron XRD data of (a) BiG1, and (b) BiG4.

Table S1. The refined lattice parameters of the Aurivillius-phase samples, as obtained from the room temperature XRD data.

Sample/		Lattice parameters			GOF
phase	***a*** **(Å)**	***b*** **(Å)**	***c*** **(Å)**	***V*** **(Å^3)**	χ^2
BFTO/A2$_1$am	5.4592(1)	5.4327(1)	41.2204(9)	1222.55(5)	1.28
BiG1/A2$_1$am	5.4302(1)	5.4121(1)	41.2628(6)	1212.68(3)	1.32
BiG2/A2$_1$am	5.414(1)	5.405(1)	41.562(1)	1216.21(6)	2.66
/B2cb	5.433(6)	5.407(3)	32.902(2)	966.54(5)	
BiG3/A2$_1$am	5.413(1)	5.394(0)	41.709(1)	1217.81(3)	2.73
/B2cb	5.431(4)	5.403(2)	32.933(12)	966.38(3)	
BiG4/A2$_1$am	5.414(0)	5.401(1)	41.614(9)	1216.83(2)	2.46
/B2cb	5.431(1)	5.401(2)	32.929(2)	965.90(3)	
BiG5/A2$_1$am	5.393(1)	5.383(1)	42.092(9)	1221.96(5)	2.74
/B2cb	5.399(1)	5.391(0)	32.940(2)	958.75(3)	

a, *b* and *c* – the lattice parameters, *V* – the unit cell volume, χ^2 – the goodness of fit (GOF)

Table S2[1]. Refined structural parameters and selected bond distances and bond angles for the 4-layered $A2_1am$ and 3-layered $B2cb$ Aurivillius phases, as obtained by Rietveld refinement of the room-temperature synchrotron XRD data of the BiG1 and BiG4 samples.

$A2_1am$	a = 5.4292(4) Å, b = 5.4146(4) Å, c = 41.294(2) Å, V = 1213.9(1) Å^3				
Atom	**Wyckoff positions**	**Fractional Coordinates**			**U_{iso} (x 100)**
		x	y	z	(Å^2)
Bi/Gd(1)	4a	0.25[a]	0.247(5)	0	1.03(4)
Bi/Gd(2)	8b	0.235(8)	0.243(2)	0.1043(1)	1.61(2)
Bi(3)	8b	0.231(5)	0.267(3)	0.2189(1)	1.36(2)
Ti/Fe(1)	8b	0.292(6)	0.247(9)	0.4511(4)	0.63[b]
Ti/Fe(2)	8b	0.270(9)	0.255(9)	0.3469(4)	0.63[b]
O(1)	4a	0.320[c]	0.190[c]	0.5 [c]	0.42[b]
O(2)	8b	0.616[c]	0.539[c]	0.0525[c]	1.56[b]
O(3)	8b	0.300[c]	0.310[c]	0.4005[c]	0.91[b]
O(4)	8b	0.490[c]	0.480[c]	0.1357[c]	0.72[b]
O(5)	8b	0.306[c]	0.226[c]	0.3066[c]	1.72[b]
O(6)	8b	0.525[c]	0.467[c]	0.2434[c]	0.56[b]
O(7)	8b	0.011[c]	0.970[c]	0.0403[c]	1.47[b]
O(8)	8b	0.040[c]	0.037[c]	0.1487[c]	0.55[b]
Bond lengths (Å):					
Bi/Gd(1)-O(1)	2.36(5)	Bi(1)-O(2)	2.56(2)	Bi(1)-O(7)	2.48(1)
	2.43(5)		3.34(5)		2.59(3)
	3.04(7)				
	3.11(7)				
Bi/Gd(2)-O(2)	2.52(1)	Bi(2)-O(3)	2.38(7)	Bi(2)-O(4)	2.34(6)
	3.38(1)		3.09(4)		2.43(8)
				Bi(2)-O(7)	3.25(8)
Bi(3)-O(5)	2.53(7)	Bi(3)-O(6)	2.09(4)	Bi(2)-O(8)	2.39(4)
	2.73(6)		2.17(8)		2.89(9)
	3.14(1)		2.30(8)		
	3.30(4)		2.76(8)	Bi(3)-O(8)	3.32(1)
Bi(3)-Bi(3)	3.71(2)	O(6)-O(6)	2.73(2)		
Bond angles (deg.):					
O(3)-O(1)-O(3)	161.8(2)		O(1)-O(3)-O(5)	164.2(3)	
O(7)-O(2)-O(7)	150.6(3)		O(8)-O(4)-O(8)	148.9(1)	
Ti/Fe(1)-O(1)-Ti/Fe(1)	160.6(6)	Ti/Fe(1)-O(3)-Ti/Fe(2)	162.2(3)		
Ti/Fe(1)-O(7)-Ti/Fe(1)	155.1(2)	Ti/Fe(2)-O(8)-Ti/Fe(2)	162.9(2)		
Octahedral tilts (deg.):					
O(1)-O(3):O(6)-O(6)	9.1(2)	O(3)-O(5):O(6)-O(6)	6.7(2)		
***R*-factors:**	R_w = 6.4, R_p = 9.2				

---

[1] A slight difference in lattice parameters obtained by full profile matching method and those refined using the Rietveld method is brought by the different X-ray sources used (standard laboratory unit *vs*. high-energy synchrotron source), providing distinctive accuracy and resolution, specifically, for determining oxygen positions in bismuth-layered Aurivillius structures.

Table S2 (cont.)

B2cb	a = 5.3994(8) Å, b = 5.3907(7) Å, c = 32.940(2) Å, V = 958.8(2) Å^3				
Atom	**Wyckoff positions**	**Fractional Coordinates**			**U$_{iso}$ (x 100)**
		x	y	z	(Å^2)
Bi(1)/Gd(1)	8b	0.13511[a]	0.994(9)	0.0659(2)	2.5(3)
Bi(2)	8b	0.150(16)	0.015(8)	0.2098(2)	1.9(2)
Ti/Fe/Co/Nb(1)	4a	0.100(13)	0	0.5	0.6[b]
Ti/Fe/Co/Nb(2)	8b	0.125(15)	0.96(2)	0.3719(5)	0.6[b]
O(1)	8b	0.3207[d]	0.2299[d]	0.0057[d]	1.5[b]
O(2)	8b	0.3783[d]	0.2527[d]	0.2519[d]	1.5[b]
O(3)	8b	0.0839[d]	0.0605[d]	0.4406[d]	1.5[b]
O(4)	8b	0.0931[d]	0.9700[d]	0.3174[d]	1.5[b]
O(5)	8b	0.3804[d]	0.2674[d]	0.1115[d]	1.5[b]
O(6)	8b	0.3209[d]	0.2216[d]	0.8793[d]	1.5[b]
Bond lengths (Å):					
Bi/Gd(1)-O(1)	2.53(6) 2.85(8) 2.97(9)	Bi/Gd(1)-O(3)	2.41(3) 3.46(6)	Bi/Gd(1)-O(6)	2.39(7) 2.91(7)
Bi(2)-O(2)	2.27(2) 3.31(6)	Bi(2)-Bi(2) O(2)-O(2)	3.70(2) 2.72(3)	Bi(2)-O(4)	2.61(11) 2.97(4)
Bond angles (deg.):					
O(3)-O(3)-O(4)	163.7(4)		O(1)-O(1)-O(1)	164.1(2)	
Ti/Fe(1)-O(3)-Ti/Fe(1)	158.4(1)	Ti/Fe(2)-O(3)-Ti/Fe(2)	158.4(1)		
Ti/Fe(1)-O(1)-Ti/Fe(1)	160.0(2)	Ti/Fe(2)-O(5)-Ti/Fe(2)	143.3(5)		
Octahedral tilts (deg.):					
O(3)-O(3):O(2)-O(2)	9.4(1)	O(3)-O(4):O(2)-O(2)	6.9(1)		
***R*-factors:**	R_w = 11.4, R_p = 16.6				

[a] Fixed to define origin of polar axis.
[b] U$_{iso}$ fixed as Rietveld refinement tends towards negative values.
[c] Oxygen coordinates taken from *Ref.* [18].
[d] Oxygen coordinates taken from *Ref.* [8].

Notes to the Rietveld analysis of the XRD data and Table S2:

The initial structural data for the four-layered $A2_1am$ phase in BiG1 and the three-layered $B2cb$ phase in BiG4 were taken from our previous studies on Gd-substituted BFTO [18] and multiferroic $Bi_{3.25}La_{0.75}(Fe_{0.5}Co_{0.5})_{0.25}Ti_{2.5}Nb_{0.25}O_{12}$ ceramics [8], respectively. The B-site cations were set to occupy the same position in the centre of each oxygen octahedron in the perovskite-like layers with fixed Ti occupancy (3/4 in $A2_1am$ phase and nearly 1/2 in $B2cb$ phase). The occupancies of Fe, Co and Nb were adjusted in the refinement of both phases in the way to reflect the nominal doping level of the Co and Nb ions. The isotropic atomic displacement parameters (ADPs) of these ions were constrained to be equivalent. The positions of oxygens with ADPs in both structures were taken from *Refs.* [8,18] and not further refined in order to stabilize the refinements. It is worth mentioning that in the doped samples, the accuracy of the refinement decreased by an order due to the structural similarity of the main orthorhombic phases $A2_1am$ and $B2cb$. Also, the values of the GOF parameter are about twice of the value of the single phase BiG1, although they are yet representing a good match between experimental and calculated XRD patterns.

From the modelled crystal structure (Figs. S4(a) and S4(b)) of $Bi_{4.3}Gd_{0.7}FeTi_3O_{15}$ and $Bi_{4.3}Gd_{0.7}(Fe_{0.5}Co_{0.5})_{1.3}Ti_{2.4}Nb_{0.3}O_{15}$, the size of perovskite-like slabs, the *a* parameter, in the four- and three- layered Aurivillius phases was estimated to be ~4.307 Å and ~4.335 Å, respectively. The fluorite-like $(Bi_2O_2)^{2+}$ layer remains in both the four- and three-layered Aurivillius phases practically identical within the range of the experimental error (the Bi-Bi bond length is about 3.7 Å and the distance between oxygen ions is about 2.7 Å). Therefore, since the unconstrained *a* parameter of the fluorite-like $(Bi_2O_2)^{2+}$ layer in both the four- and three-layered Aurivillius phases does not change (~3.70 Å), this suggests that the perovskite-like slabs of the $B2cb$ phase in the BiG5 sample are under larger compressive stress than those of the $A2_1am$ phase. As a result, the larger size mismatch between perovskite-like slabs and fluorite-like layers (interlayer mismatch) in the doped samples is relieved by the larger tilting distortion of the oxygen octahedra. The comparison of the non-bonded contact angles O3-O1-O3 in $A2_1am$ (~161.8^0) and O3-O3-O4 in $B2cb$ (~163.7^0) indicates that the tilting around the *a*-axis in the four-layered phase is again smaller than that in the three-layered phase. On the other hand, the bond angles of the B-O-B chains along the *c*-axis in the inner and outer perovskite-like layers are smaller in the three-layered structure, if compared to those of the four-layered phase.

By comparing the values of Bi-O bond lengths in the *ab* plane for the four- and three-layered structures (Table S2), one can see that the distance between bismuth and oxygen atoms in $B2cb$ (Bi1-O3) is about 2% longer than that in the $A2_1am$ phase (Bi1-O1≈2.36 Å). The longer Bi-O bond lengths in the *ab* plane and the smaller B-O-B bond angles along the *c*-axis in the three-layered Aurivillius phase suggest that the local environment of B-site cations in the inner perovskite-like slabs of the $B2cb$ structure differs from that in the $A2_1am$ structure. These findings are supportive of the inherent mechanism of lowering crystal symmetry driven by Co-doping of Gd-substituted BFTO (SG: $A2_1am$), which is accompanied by the occurrence and growth of the three-layered *B*2*c* phase with the increased octahedral tilting. The introduction of the donor Nb ions at the B-sites of perovskite-like layers balances the electrical neutrality disrupted by Co doping, favouring the three-layered BTO-like Aurivillius phase.

Mössbauer spectra analysis

Table S3. Hyperfine interactions parameters of BiG1, BiG3 and BiG5 ceramics, as obtained from the numerical fitting of the Mössbauer spectra collected at 300 K.

Sample	**Component**	**IS (mm/s)**	**QS (mm/s)**	**Δ (mm/s)**	**B_{eff} (T)**	**A (%)**
BiG1	Doublet D1	0.35	0.50	-	-	90.4
	Doublet D2	0.25	0.72	-	-	9.6
BiG3	Doublet D1	0.29	0.27	-	-	56
	Doublet D2	0.21	0.71	-	-	43
	Sextet	0.26	-	0.08	40.3	1
BiG5	Doublet D1	0.28	0	-	-	19
	Doublet D2	0.23	0.65	-	-	47
	Sextet	0.29	-	-0.04	43.5	34

IS – isomer shift relative to α-iron, QS – quadrupole splitting of the doublet, Δ - quadrupole shift of the sextet, B_{eff} – effective hyperfine magnetic field induction, A – integral intensities ratio

SQUID magnetometry

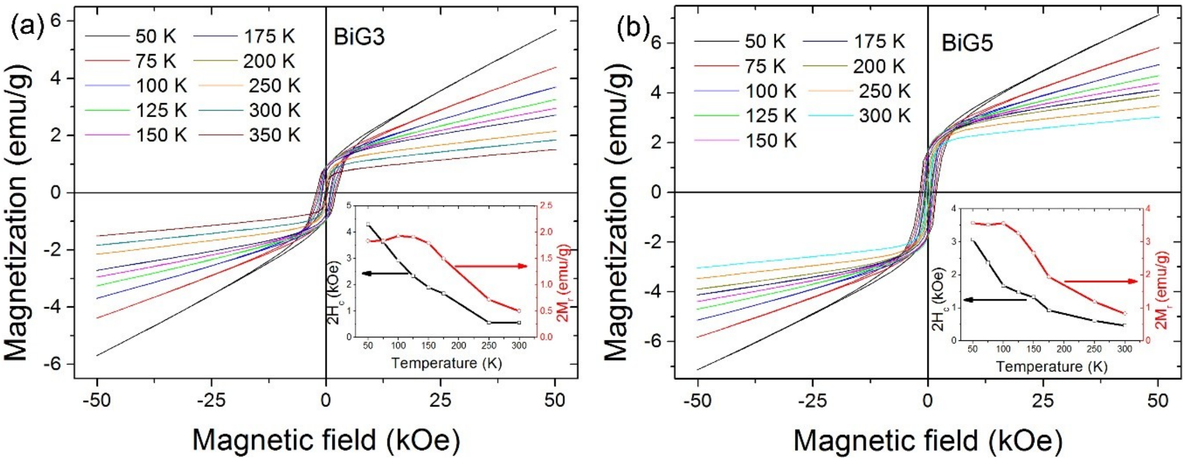

Figure S3. The magnetization *vs*. magnetic field hysteresis loops of (a) BiG3, and (b) BiG5, as recorded at different temperatures between 50 K and 350 K. The insets show the temperature dependences of the remanent magnetization ($2M_r$) and coercive field ($2H_c$) for the respective samples.

S-TEM HAADF imaging

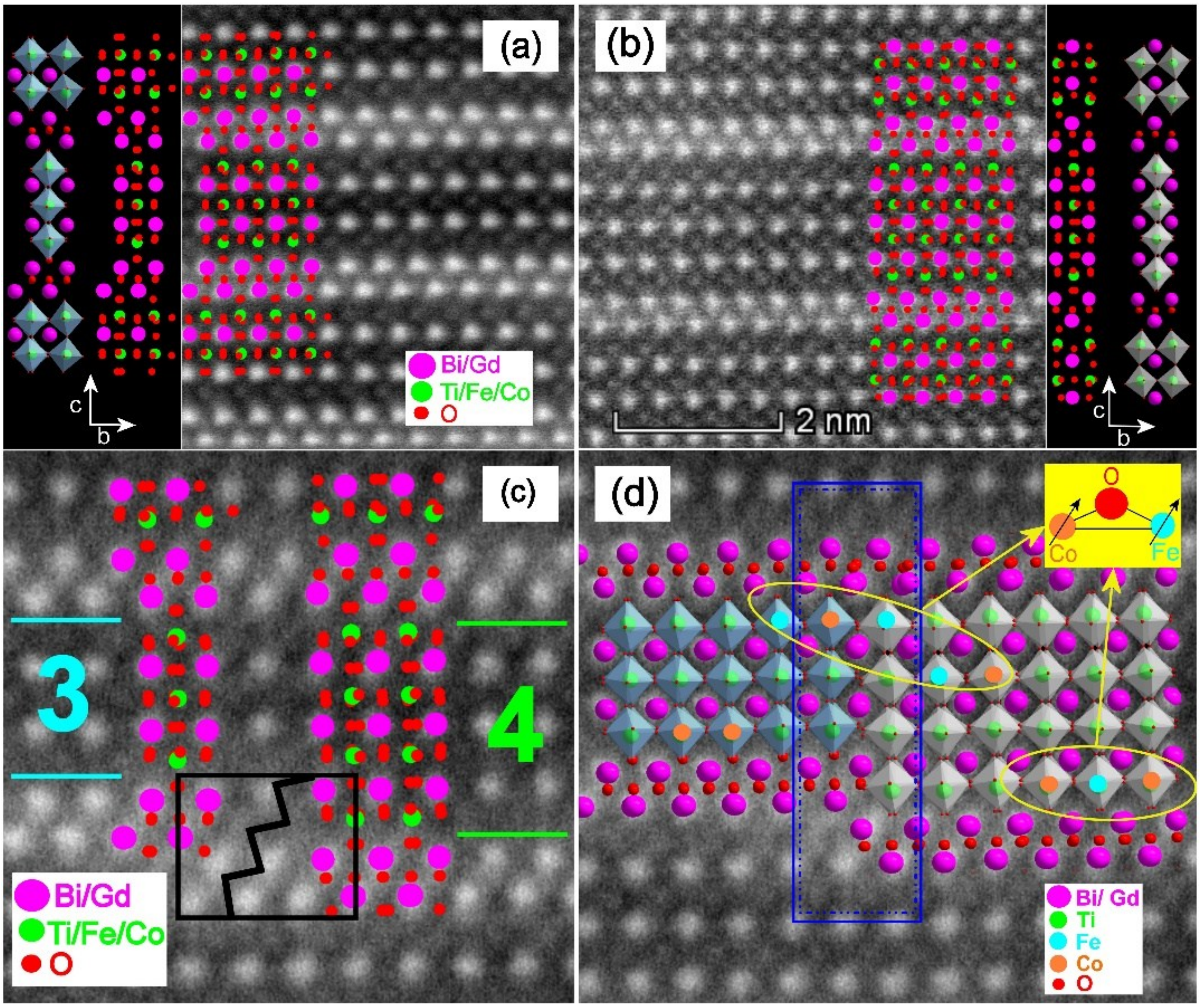

Figure S4. Atomic scale resolution images of (a) the three-layered *B*2*cb* phase, and (b) the four-layered $A2_1am$ phase (overlapped by the respective 2D and 3D sketches of the crystal structure). (c) The enlarged HAADF image nearby the Bi_2O_2 layer defect demonstrating the intergrowths of the three- and four-layered phases. (d) The illustration of the ferromagnetic Fe-O-Co clustering driven by the nanoscale structural modulation at the interface of the two phases.

NEXAFS and EXAFS analysis

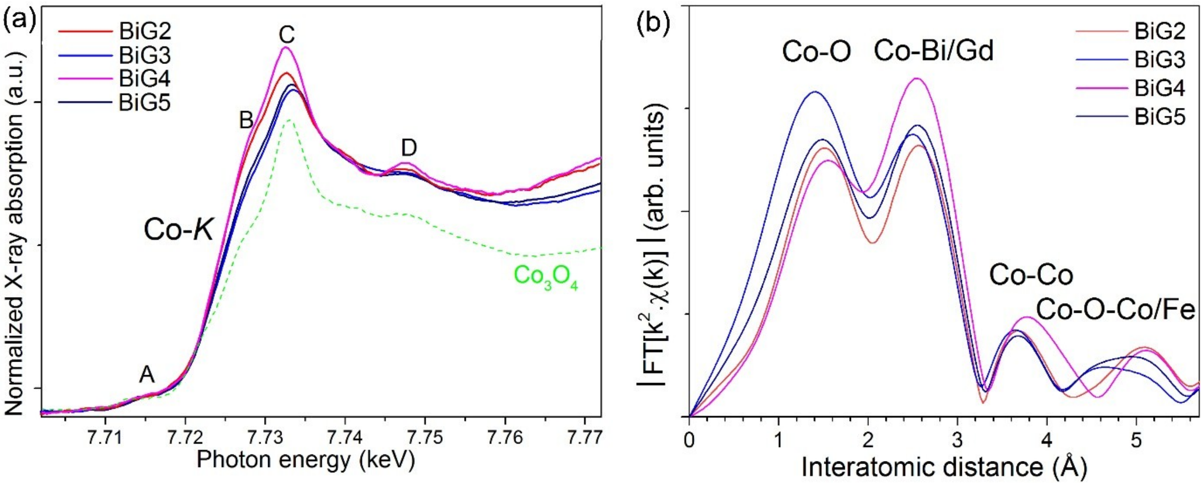

Figure S5. (a) The room-temperature XANES Co *K*-edge spectra of the BiG1-BiG5 samples. (b) Fourier transform (FT) of the EXAFS function, $\chi(k)$, into real space for the BiG1-BiG5 samples.

ZFC/FC magnetization

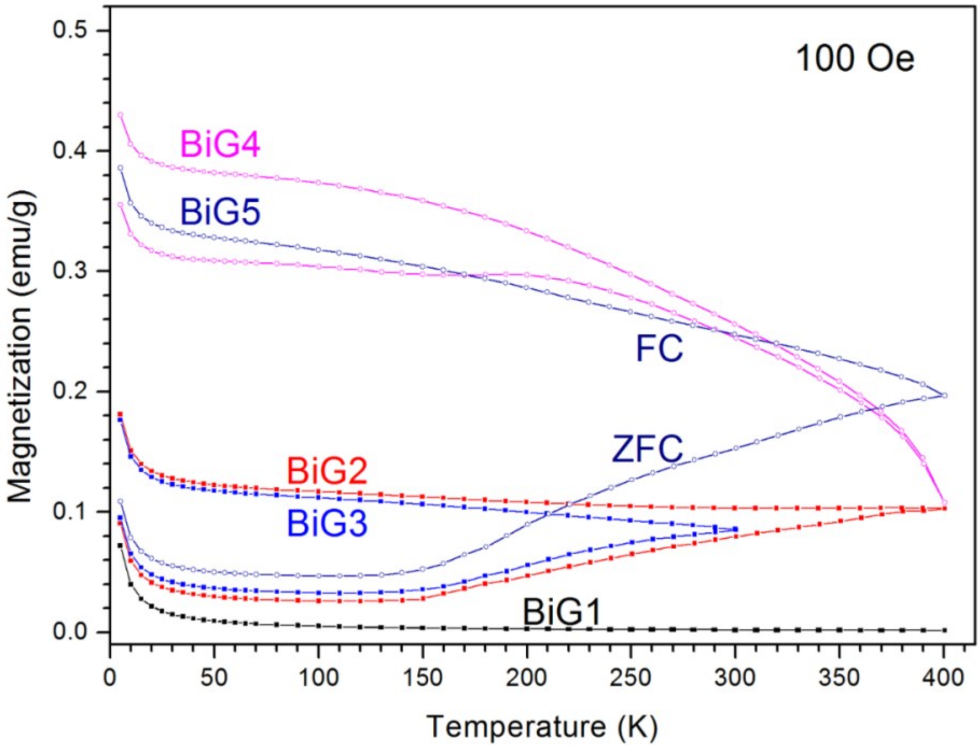

Figure S6. Magnetization as a function of temperature of the BiG1-BiG5 samples, as recorded at 100 Oe in the temperature range of 5 K-400 K.

Scanning electron microscopy analysis

Fig. S8(a) and S8(b) show cross-sectional SEM images of the polished, chemically etched surfaces of BiG1 and BiG5 ceramics, respectively. From the figure, one can see that both samples are formed of plate-like grains, characteristic of Aurivillius-phase materials [5]. The growth habit is determined by the particular crystalline (layered) structure which promotes preferential growth of grains in directions perpendicular to the stacking *c*-axis of the perovskite-like layers. In addition, the platelets of BiG1 ceramics are much smaller (the average length and width are about 1-1.5 μm and 0.2-0.3 μm, respectively) than those of BiG5 ceramics (average length: 4-5 μm and average width: 1 μm), indicating that the Co substitution and Co/Nb-codoping can effectively promote the grain growth in BFTO-derived materials. It should be noted that the Gd, Fe, Co and Nb elements also exist in the three-layered structure, implying that the *B*2*cb* phase is not pure $Bi_4Ti_3O_{12}$ but rather of the $(Bi,Gd)_4(Ti,Nb)_2(Fe,Co)O_{12-\delta}$-type compound.

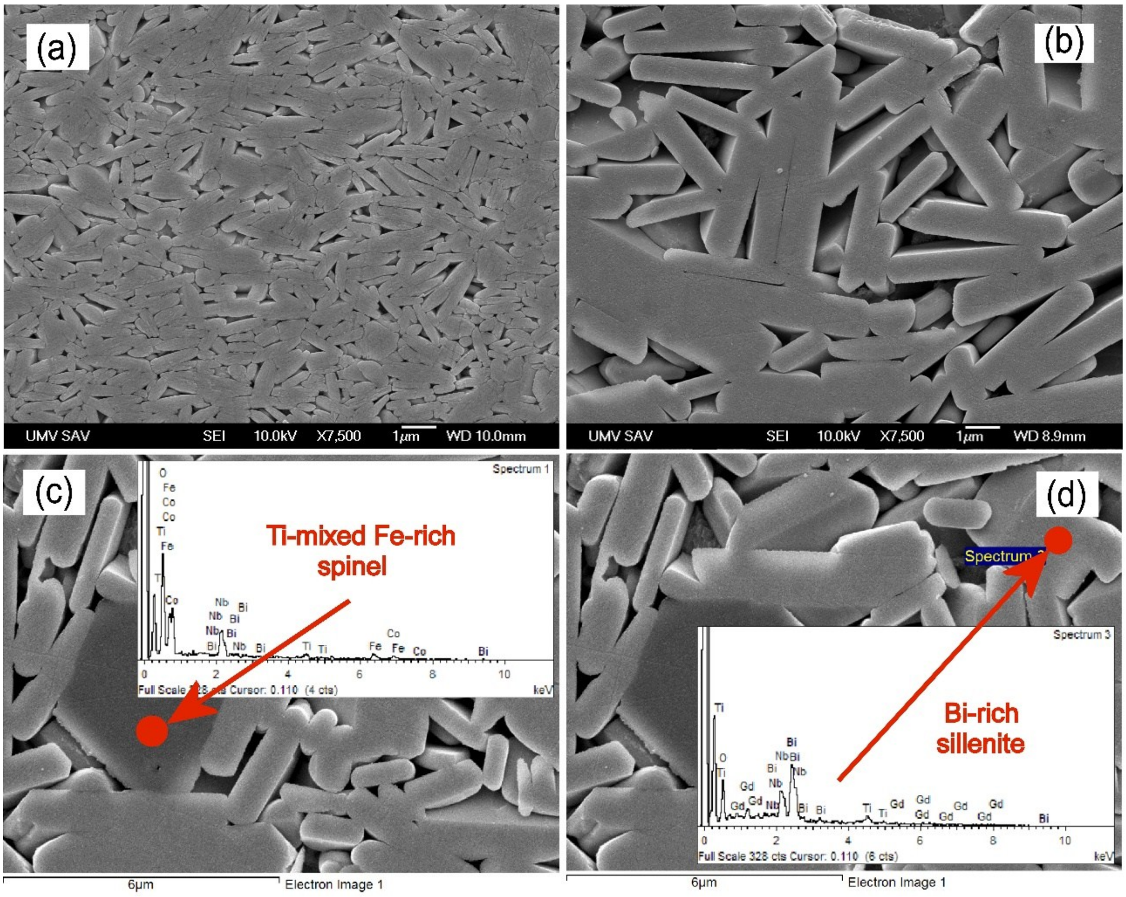

Figure S7. SEM images of (a) BiG1, and (b) BiG5 ceramics (magnification: x7500). (c, d) The micrograph demonstrating at a higher magnification (x20000) the existence of two different types of impurities in the BiG5 ceramics; (c) Ti-mixed Fe-rich spinel ferrite, and (d) Bi-rich sillenite-type particle. The insets of (c) and (d) are the EDX spectra of the impurities.

The presence of two different types of secondary phases in the doped BiG5 sample is evidenced in the micrographs obtained at a higher magnification (Fig. S8(c) and S8(d), magnification: 20000x). While the volume fraction of the cubic impurities (dark particles, size ~ 3-4 μm) is less than 3.5% (estimated from a series of micrographs, not shown here), i.e., below the detection limit of the XRD technique, the smaller octahedral-like shaped particles of about 2 μm occupy nearly 10 vol.% of the doped sample. Following the results of our XRD analysis, the latter impurities are supposed to be Bi-rich sillenite-type particles with composition close to $Bi_{12}TiO_{20}$. Semi-quantitative EDX analysis (spot scan), indeed, confirmed that the atomic ratio of the A-site cations (Bi+Gd) to the B-site cations (Ti+Nb) in these particles is about 12:1.

The atomic ratio Co/(Fe+Ti) in the dark cubic particles was found to be close to 1, suggesting that these impurities are Ti-mixed Fe-rich spinel ferrites ($FeCo_2O_4$-like spinels) Surprisingly, the EDX analysis of the dark particles in the ceramic samples with the lower concentration of the Co added (BiG2 and BiG4 ceramics) showed that the amount of Fe atoms is almost twice of Co atoms, which indicates that a minor secondary phase in these samples is of the spinel Fe_2CoO_4-type with Fe partially replaced by the Ti atoms. The presence of spinel-type impurities in the Co-doped four-layered Aurivillius compounds has been reported in our earlier work on La-BFCT ceramics [22] and also by other research groups [19,26,32].

AC magnetic susceptibility and spin glass-like behavior

The low frequency (0.1 Hz) AC susceptibility anomaly (see Fig. 10(b)) coincides with the temperature at which the DC magnetization starts to fall (see Fig. 10(a)), thus, we define the peak point in χ''_{ac} curve as the dynamic spin freezing temperature $T_f(\omega)$. The frequency dependence of T_f is often quantified by an empirical parameter ϕ:

$$\emptyset = \frac{\Delta T_f}{T_f \Delta log_{10}(\omega)}, \quad (1)$$

which represents the relative shift of T_f per decade of $\omega/2\pi$ on a logarithmic scale. The calculated value of the parameter ϕ for the BiG3 sample is about 0.083 and compares well with the values of 0.06 in certain shape memory alloys showing the SG state [65] and 0.095 reported in disordered SG systems such as $LaCo_{0.5}Ni_{0.5}O_3$ [66]. Accordingly, it can be proposed that the initial frequency shift of 0.083 better characterizes our Aurivillius system as the so called cluster glass. In such a system of spin-clusters, a strong inter-cluster interaction can give rise to spin glass-like cooperative freezing at the critical spin-glass temperature T_{SG}, which is associated with the characteristic time $t=1/\omega$ (t corresponds to the maximum relaxation time τ, $\tau=2\pi/\omega$). Thus, as $\omega\rightarrow 0$, $T_f(\omega)$ is expected to settle down to a "static limit", T_{SG}.

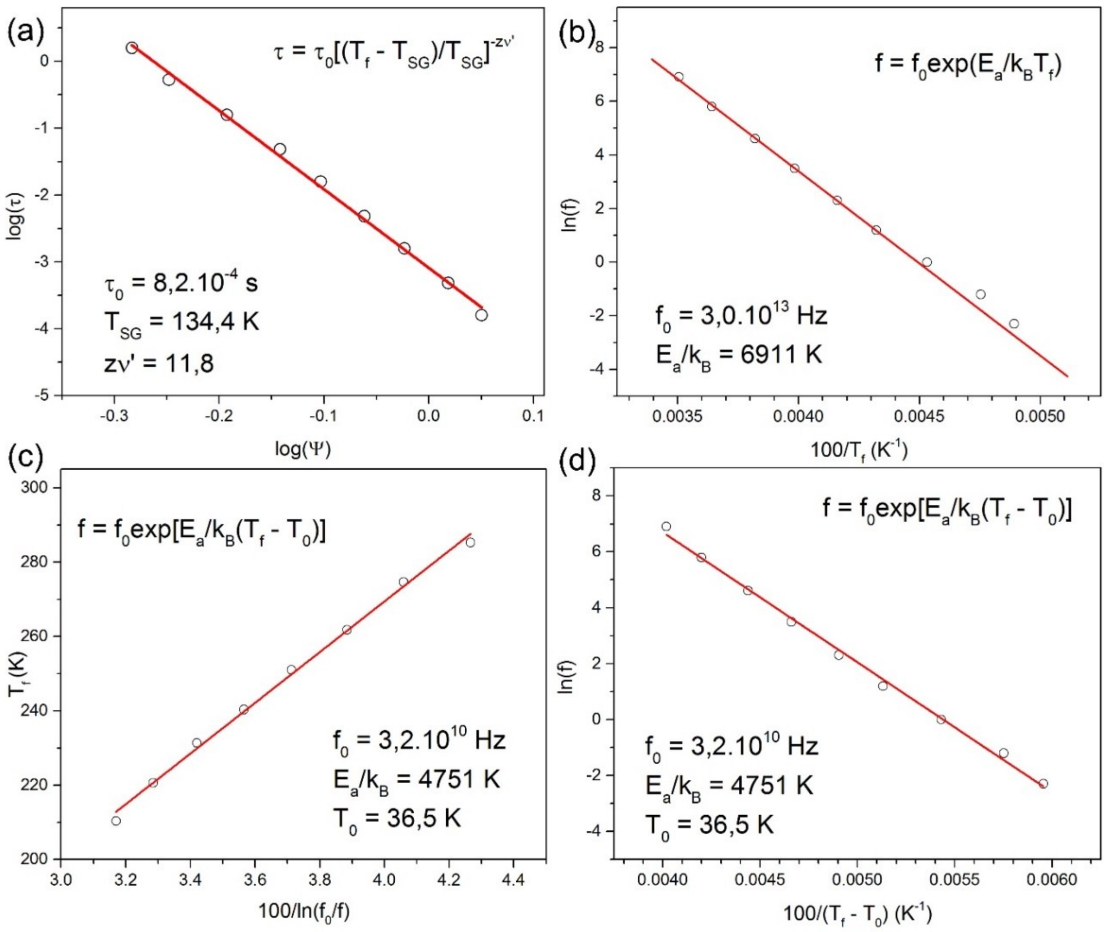

Figure S8. (a) The frequency dependence of freezing temperature plotted as log(τ) *vs*. log (ψ), where the reduced temperature $\psi = (T_f - T_{SG})/T_{SG}$. The red solid line represents the fit to the power law divergence. (b) The frequency dependence of freezing temperature plotted as ln(f) *vs*. 100/T_f. The red solid line represents the fit to the Arrhenius law. (c) The frequency dependence of freezing temperature plotted as T_f *vs*. 100/ln(f_0/f). The red solid line represents the fit to the Vogel-Fulcher lav. (d) The frequency dependence of freezing temperature plotted as ln(f) vs. 100/(T_f-T_0). The red solid line represents the fit to the Vogel-Fulcher law.

On further analysis of the AC data, in the vicinity of T_{SG}, the T_f was found to obey the critical slowing down dynamics governed by the relation:

$$\tau = \tau_0 \left(\frac{T_f}{T_{SG}} - 1 \right)^{-zv'}, \qquad (2)$$

where τ_0 is the shortest relaxation time available to the system, T_{SG} is the critical SG transition temperature, z is the dynamic critical exponent, and v' is the critical exponent of the correlation length. For a convenience, it is useful to rewrite Eq. 2 to the equivalent linearized form as:

$$ln(\tau) = ln(\tau_0) - zv' ln(\psi), \qquad (3)$$

where $\psi=(T_f-T_{SG})/T_{SG}$. The slope and intercept of ln(τ) *vs.* ln(ψ) plot can, thus, be used to estimate τ_0 and zv'. A log-log plot of inverse frequency (τ) *vs.* reduced temperature (ψ) of BiG3 is shown in Fig. S8(a). The value of T_{SG} was determined by extrapolating the T_f *vs.* $f^{1/zv'}$ to zero frequency, which gives T_{SG}=134.4 K (see the inset of Fig. S9). The solid red line in Fig. S8(a) represents the fit to the power law divergence (Eq. 2). The best fit to the experimental data (solid circles in Fig. S8(a)) yields the following fitting parameters: $\tau_0=8.2\times10^{-4}$ s, T_{SG}=134.4 K and zv'=11.8. Fig. S9 clearly demonstrates the validity of the power law (green dashed line) over the whole experimental temperature range. The value of the critical dynamical exponent zv' is in good agreement with that reported for cluster glasses.[67,68] In addition, rather large τ_0 suggests a cluster-glass nature of the Aurivillius material, too. The slower relaxation, if compared to a conventional spin glass ($\tau_0 \sim 10^{-10}$-10^{-13} s [62]), indicates that the low-temperature SG-like phase of BiG3 is composed of randomly distributed ferromagnetic clusters. Similar cluster glass effect, induced by disorder, has been reported in doped manganites and nanocrystalline alloys.[69,70]

The cooperative dynamics due to the inter-cluster interactions is also evident from the departure of the frequency dependence of T_f from the Néel-Arrhenius law (see Fig. S9, red dashed line) given by

$$\tau = \tau_0 exp\left(\frac{E_a}{k_B T_f} \right), \qquad (4)$$

where E_a is the activation energy and k_B is the Boltzmann constant. A significant deviation from the expected linear behaviour at low frequencies confirms that the dynamics is not simply associated with single-spin flips, but rather reflects a cooperative character of the freezing process. We made an attempt to estimate the activation energy E_a by fitting the data above 10 Hz (red solid line in Fig. S8(b)) by an Eq. 4, yielding E_a/k_B=7876±188 and τ_0=5.3×10^{-15} s which are totally unrealistic values.

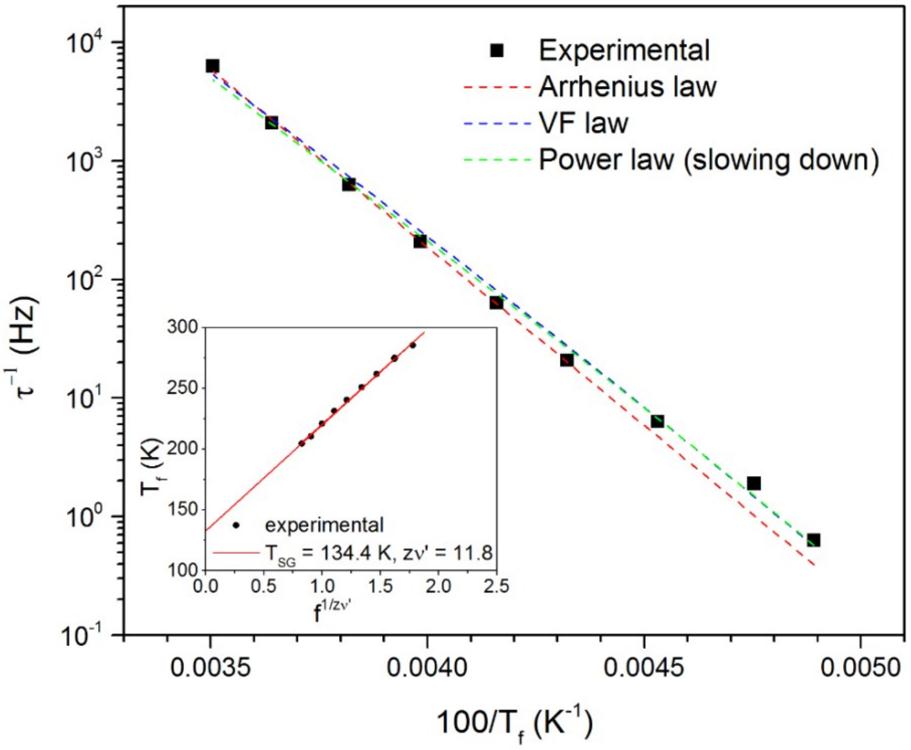

Figure S9. Fitting the χ''_{ac} maxima by the Arrhenius law (red dashed line), the Vogel-Fulcher law (blue dashed line) and the power law (Eq. 2, green dashed line). The straight line in the inset defines the value of the critical exponent $z\nu'$ and the critical spin-glass temperature T_{SG}.

On the other hand, the empirical Vogel-Fulcher law [62] which takes into account the interactions among spin clusters:

$$\tau = \tau_0 exp\left(-\frac{E_a}{k_B(T_f - T_0)}\right), \tag{5}$$

where T_0 is the Vogel-Fulcher temperature which represents the measure of inter-cluster interaction strength and describes the relaxation behaviour in the vicinity of the SG-like transition satisfactorily, as shown in Fig. S8(c) and S8(d). A good linear fit of the Vogel-Fulcher law to the experimental data with physically meaningful parameters τ_0=3.1x10^{-11} s, T_0=36.5 K and E_a=0.41 eV was obtained from the slope and intercept of T_f *vs*. 1/$ln(f_0/f)$ plot. According to the criterion introduced by Tholence [71], $T^*=(T_f-T_0)/T_f$ should be very small for SG states. Our value of *T** for the BiG3 sample is about 0.82, which is an order magnitude higher than those reported for canonical spin glasses or ideal spin glasses [62], but is comparable to the values obtained for systems with a progressive freezing of clusters [72].

From the AC susceptibility analysis, one can infer that the glassy magnetic behavior of the Aurivillius compounds originates from competing antiferromagnetic and ferromagnetic interactions within and between the cooperative Fe-O-Co polar clusters, which support the presence of Co^{3+} ions in the low spin (LS) state, Co^{3+} (S=0). According to Goodenough-Kanamori rules for super-exchange interactions [52], a disordered distribution of LS Co^{3+} and high spin Fe^{3+} would result in the frustration between the ferromagnetic double exchange (Co-Fe) and the antiferromagnetic superexchange (Co-Co and Fe-Fe) interactions. The presence of low concentrations of Co^{2+}, as indicated by the XAFS study, in the high spin (S=3/2) electronic configuration further rationalize the spin glass behavior at low temperatures, as the HS Co^{2+} - HS Co^{2+}, HS Co^{2+} - LS Co^{3+} interactions are antiferromagnetic [52].

Dielectric and ferroelectric properties

To investigate the dielectric behaviour of the Aurivillius materials near the Curie point and at the same time to confirm the temperature of the ferroelectric-to-paraelectric phase transition determined by DSC, we performed the dielectric property measurements in a temperature window of 800 K – 1200 K.

For dielectric and ferroelectric characterization, the sintered pellets were first thinned to a thickness of about 0.5 mm by wet grinding (#1200 SiC paper, Struers GmbH, Germany) followed by polishing (DP-Suspension P, Struers GmbH, Germany), and then major faces of the disks were electroded with fired-on silver paste (#7095, DuPont Ltd., UK). The dielectric properties were measured using a precision impedance analyzer (#4294A, Agilent, Japan) attached to a home-made laboratory furnace. Ferroelectric characterization was performed with a ferroelectric tester (NPL, Teddington, UK) with the testing frequency of a triangular voltage waveform of 10 Hz.

Fig. S10 shows the temperature dependencies of the relative dielectric permittivity (ε_r) of the Co-free BiG1 sample and the representative Co-doped and Co/Nb- codoped ceramics (BiG2, BiG3 and BiG5), as obtained at three different frequencies. For all the samples, ε_r first increases slowly with temperature and then above 1070 K it starts to grow abruptly, reaching a maximum at a temperature close to 1100 K. The dielectric anomaly (peak in ε_r *vs.* T curve) is frequency independent and the temperature of the permittivity maximum matches well with that of the endothermic DSC peak for each composition (see Fig. 1b). In our earlier work we have demonstrated that the dielectric permittivity peak of similar four-layered $Bi_{4.25}La_{0.75}Ti_3Fe_{0.5}Co_{0.5}O_{15}$ Aurivillius ceramics at about 1100 K corresponds to the ferroelectric Curie temperature, T_c^{FE}.[22] Lomanova *et al.* have reported on second-order-type ferroelectric phase transitions occurring between 900 K and 1100 K in multi-layered Aurivillius compounds.[35] Here, the ferroelectric Curie temperature T_c^{FE} decreases from 1103 K (BiG1) to 1098 K (BiG3) as the amount of the Co added is increased from x=0 to x=0.5. Both these temperatures are higher than that of pure BFTO (~1023 K [30]), but they are close to the ferroelectric Curie temperature of BLFCT ceramics (T_c^{FE} ~1060 K [22]) where we used more polarizable lanthanum atoms as the A-site substituent instead of gadolinium. The additional partial replacement of Ti^{4+} ions by Nb^{5+} ions shifts the T_c^{FE} to lower temperatures, leading to the ferroelectric transition of BiG5 at about 1095 K.

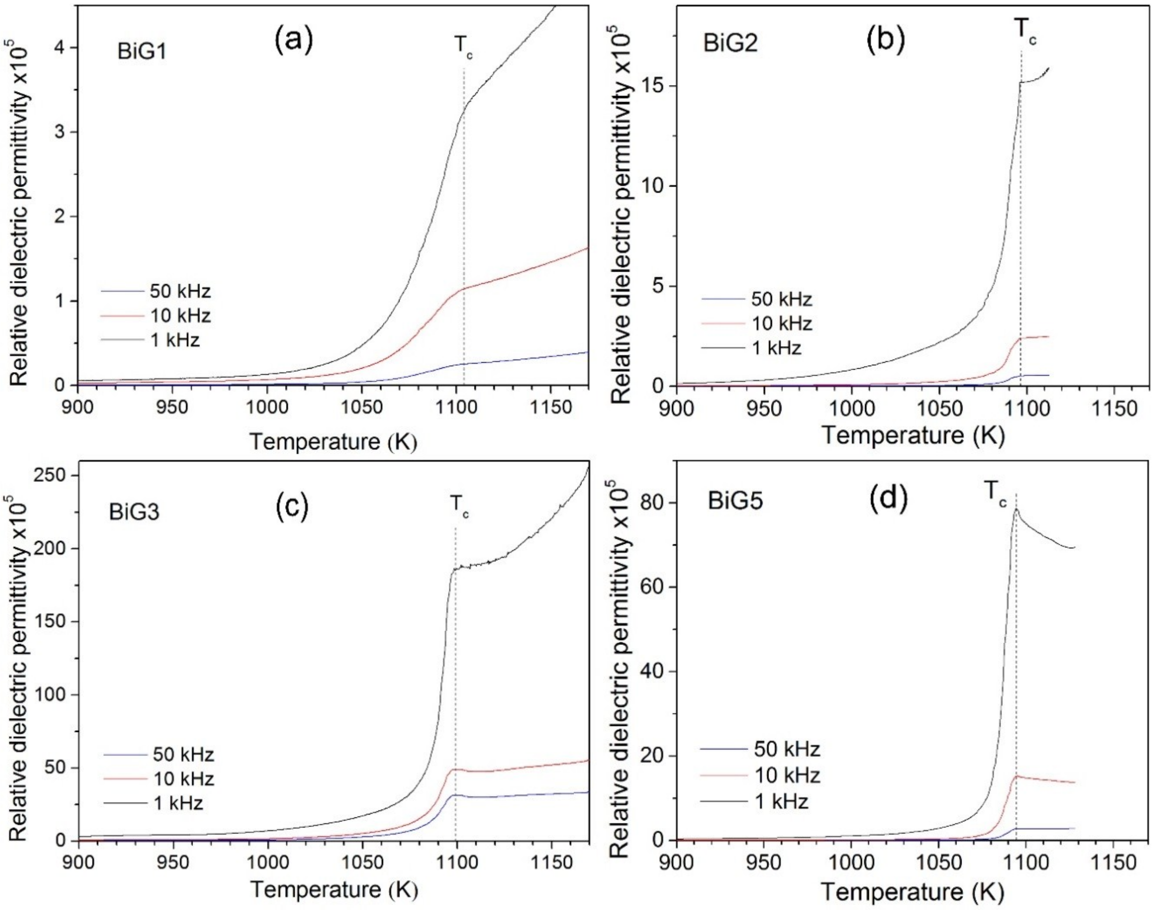

Fig. S10. Temperature dependence of the relative dielectric permittivity of (a) BiG1, (b) BiG2, (c) BiG3, and (d) BiG5 samples, as obtained at three different frequencies (1 kHz, 10 kHz and 50 kHz).

Below T_c^{FE}, the dielectric response of BFTO-derived Aurivillius multiferroics with 3*d* transition metal ions at B sites is often perturbed by extrinsic effects such as interfacial polarization [73] and two-site polaron hoping mechanism [21] originating from charge defects (e.g., oxygen vacancies, valence fluctuation of Fe/Co ions). As a consequence (of a change in conductive mechanism), a bump shoulder in the ε_r-T plot has been typically observed at temperatures around 600 K, and this broad peak was found to decrease and shift toward a higher temperature when the testing frequency is increased.[28]

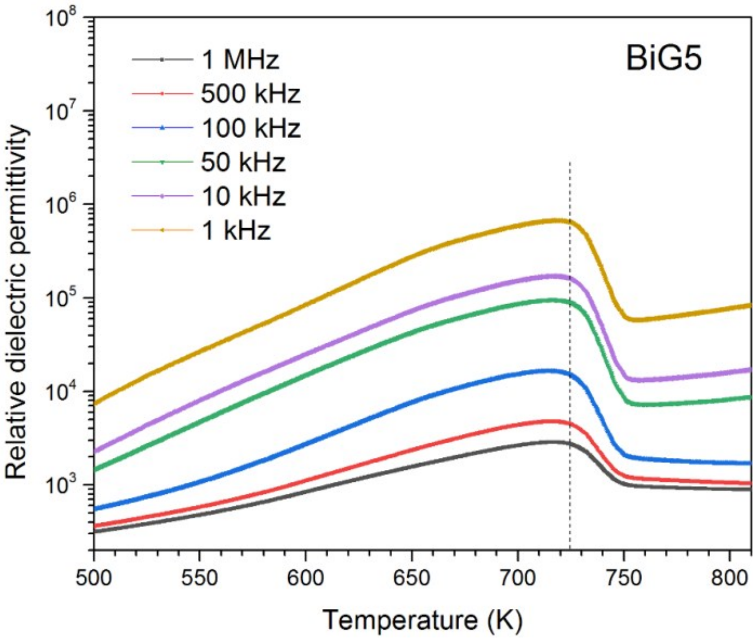

Figure S11. Temperature dependence of the relative dielectric permittivity of the BiG5 sample, as recorded in the temperature interval 500-800 K.

To investigate the dielectric response of our samples for a possible relaxation from extrinsic effects at lower temperatures, the relative dielectric permittivity and loss tangent of the samples were investigated in the temperature range 500-800 K at 1 kHz, 10 kHz, 50 kHz, 100 kHz, 500 kHz and 1 MHz. The representative plot for the BiG5 sample is shown in Fig. S11. From the figure, one can see that there is a peak in the temperature dependence of ε_r, but its maximum at about 725 K is independent on the frequency. This temperature is much higher than that of the ferrimagnetic-to-paramagnetic temperature of the spinel oxide $FeCo_2O_4$ (~460 K [49]) and lower than T_c of single phase $CoFe_2O_4$ (~785-860 K [74]), but close to the Curie temperature of the nonstoichiometric $Co_{1.2}Fe_{1.8}O_4$ $[Co^{2+}_{0.5}Fe^{3+}_{0.5}(Co^{2+}_{0.5}Co^{3+}_{0.2}Fe^{3+}_{1.3})O_4]$

spinel (T_{cm}=714 K [74]), which is known of the presence of valence fluctuations of the magnetic atoms. It should be noted that the magnetic moment of this kind of spinel is the smallest (~2.7μ_B) of all ferrites in the $Co_xFe_{3-x}O_4$ and $Co_{2-x}Ti_{1-x}Fe_{2x}O_4$ series [74,75], and thus a small amount (below the detection limit of the X-ray diffractometer) of this magnetic impurity, if present, hardly can contribute significantly to the measured magnetization at room temperature (M_s~3.5 emu/g). On the other hand, the mixed valence state of magnetic cations in the spinel oxide, as mentioned above, could be partially responsible for leaky polarization *vs.* electric field (P-E) hysteresis loops.

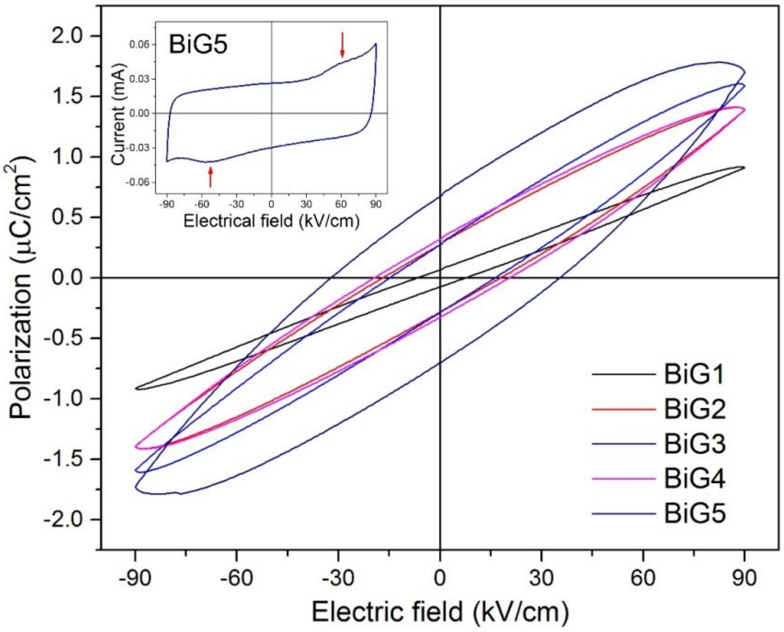

Figure S12. Polarization *vs*. electric field curves of the BiG1-BiG5 samples (at 10 Hz). The red arrows in the inset point to broad peaks on the field-dependent electrical current, indicating ferroelectric switching in BiG5.

Fig. S12 displays the P-E curves of all the samples, as recorded at room temperature and a frequency of the applied electric field of 100 Hz. Apparently, due to a large DC conductivity, the loops are not saturated even under a high driving electric field of 90 kV/cm. The presence of structural defects and low density (~89-92% of the theoretical density) caused the dielectric break-down of the samples when the field above 90 kV/cm was applied in ferroelectric tests. It should be mentioned that such low-quality “banana-type” P-E loops are quite usual for multiferroic BFTO-derived systems, where conductive Fe ions together with oxygen vacancies contribute to the increased electrical conduction.[19,76] The ferroelectricity in the Aurivillius materials was evidenced by observation of weak current peaks on the I-E curves (see the inset of Fig. S12).

References

[65] S. Chatterjee, S. Giri, S. K. De, S. Majumdar, Reentrant-spin-glass state in Ni2Mn1.36Sn0.64 shape-memory alloy, *Physical Review B*, 2009, **79**, 092410.

[66] M. Viswanathan, P. S. A. Kumar, Observation of reentrant spin glass behavior in LaCo0.5Ni0.5O3, *Physical Review B*, 2009, **80**, 012410.

[67] K. Vijayanandhini, C. Simon, V. Pralong, V. Caignaert, B. Raveau, Spin glass to cluster glass transition in geometrically frustrated CaBaFe4−xLixO7 ferrimagnets, *Physical Review B*, 2009, **79**, 224407.

[68] P. C. Hohenberg, B. I. Halperin, Theory of dynamic critical phenomena, *Reviews of Modern Physics*, 1977, 49, 435-479.

[69] J. Dho, W. S. Kim, N. H. Hur, Reentrant Spin Glass Behavior in Cr-Doped Perovskite Manganite, *Physical Review Letters*, 2002, **89**, 027202.

[70] I. Skorvanek, S. Skwirblies, J. Kotzler, Magnetic hardening and spin-glass phenomena in nanocrystalline FeNbB at low temperatures, *Physical Review B*, 2001, **64**, 184437.

[71] J. L. Tholence, R. Tourner, Susceptibility and remanent magnetization of a spin glass, *Journal de Physique Colloques*, 1974, **35**, C4-229-235.

[72] S. Garcia, L. Ghivelder, S. Soriano, I. Felner, Magnetization scaling in the ruthenate-cuprate RuSr2Eu1.4Ce 0.6Cu2O10-δ (Ru-1222), *European Physical Journal B*, 2006, **53**, 307-313.

[73] M. S. Wu, Z. M. Tian, S. L. Yuan, H. N. Duan, Y. Qiu, Dielectric behavior and ac conductivity in Aurivillius Bi4Ti3O12 doped by antiferromagnetic BiFeO3, *Physics Letters A*, 2012, **376**, 2062-2066.

[74] Q. C. Sun, C. S. Birkel, J. Cao, W. Tremel, J. L. Musfeldt, Spectroscopic Signature of the Superparamagnetic Transition and Surface Spin Disorder in CoFe2O4Nanoparticles, *ACS Nano*, 2012, **6**, 4876-4883.

[75] P. Nathwani, V. S. Darshane, Structural, transport, magnetic and infrared studies of the oxidic spinels Co2-xTi1-xFe2xO4, *Journal of Physics C: Solid State Physics*, 2000, **21**, 3191-3203.

[76] S. Liu, S. Yan, H. Luo, L. Yao, Z. Hu, S. Huang, L. Deng, Enhanced magnetoelectric coupling in La-modified Bi5Co0.5Fe0.5Ti3O15 multiferroic ceramics, *Journal of Materials Science*, 2018, **53**, 1014-1023.